

# Turing Pattern and Chemical Medium-Range Order of Metallic glasses

Song Ling Liu (刘松灵)<sup>1,2</sup>, Xin Yu Luo (罗新宇)<sup>1,2</sup>, Jing Shan Cao (曹景山)<sup>1,2</sup>, Zhao Yuan Liu (刘召远)<sup>3</sup>, Bei Bei Xu (许贝贝)<sup>4</sup>, Yong Hao Sun (孙永昊)<sup>1,2,5,✉</sup>, and Weihua Wang (汪卫华)<sup>1,2,5</sup>

*1. Institute of Physics, Chinese Academy of Sciences, Beijing, 100190, China.*

*2. School of Physical Sciences, University of Chinese Academy of Sciences, Beijing, 100190, China.*

*3. Shandong Computer Science Center (National Supercomputer Center in Jinan), Qilu University of Technology (Shandong Academy of Sciences), Jinan, Shandong, 250014, China.*

*4. Shanghai Institute of Microsystem and Information Technology, Chinese Academy of Sciences, Shanghai, 200050, China.*

*5. Songshan Lake Materials Lab, 523808, Dongguan, Guangdong, China and*

✉ Corresponding authors: ysun58@iphy.ac.cn

(Dated: May 10, 2023)

## Abstract

The formation of bulk metallic glass requires the constituent elements to have a negative heat of mixing but has no restrictions on its magnitude. An understanding of this issue is lacking due to the absence of a valid method for describing chemical ordering of metallic glasses. For example, the radial distribution function is ineffective in identifying the elemental preferences of packed atoms. Here, we show that using molecular-dynamics simulation, the chemical medium-range ordering of liquid alloys can be evaluated from persistent homology. This inherently arising chemical medium-range order in metallic glasses is exclusively regulated by the activation and inhibition of the constituent components, making the topology of metallic glasses a Turing pattern. The connecting schemes of atoms of the same species form three distinct regions, reflecting different correlations at the short and medium length scales, while the difference in the schemes corresponds to chemical ordering. By changing the elemental types, it is demonstrated that the chemical medium-range order strongly depends on the relative depth of the interatomic-potential wells. The study separates metallic glasses from crystals under the condition of negative heat of mixing by emphasizing their fundamental difference in interatomic potentials.

## INTRODUCTION

According to the empirical rule of Inoue, one of the prerequisites for casting bulk metallic glasses (MGs) is the negative heat of mixing ( $\Delta H_{\text{mix}}$ ) between any two elements of the constituents [1]. A negative  $\Delta H_{\text{mix}}$  suggests a bonding choice preferential to unlike species against like species, so factors like phase separation that are detrimental to glass formation during casting can be avoided. One might infer from this that giant MGs can be produced by lowering  $\Delta H_{\text{mix}}$  continuously or by choosing elements with  $\Delta H_{\text{mix}}$  of higher absolute values. Unfortunately, the truth is different: a study of 7688 alloys revealed that the critical cooling rate ( $R_c$ ) of binary MGs is only weakly correlated with the absolute value of negative  $\Delta H_{\text{mix}}$  [2, 3]. It is unclear why a negative  $\Delta H_{\text{mix}}$  is significant but its magnitude has no bearing on MG formation.

Since mixing involves chemical affinity of the elements, the task requires an understanding of the chemical ordering inside the MGs [4, 5], which implies bonding preference and how far the local chemistry departs from a random melt. Our knowledge, however, is rather limited and largely focused on the first radial-distribution-function (RDF) peak. Although many ordering characteristics describing the structural and chemical order of the first nearest neighbors are proposed [6–14], it is unclear what ordering characteristics contribute to the RDF peaks after the first one. Additionally, although the chemical affinity of the solute and solvent atoms of alloys are resembled using a variety of radii by Miracle [7, 15–17] following up with Bernal’s hard sphere model [18–22], these approaches are still insufficient to resolve the mystery of negative  $\Delta H_{\text{mix}}$  in the formation of MGs. A model emphasizing the chemical ordering is required, because configurations would change if the affinity of the alloying elements changed even though the radii are set. To understand the medium-range ordering (MRO) of amorphous materials, numerous simulation studies have been carried out [23–25], but they all have some drawbacks. The bond-angle or dihedral-angle distribution only highlights configurations of the third-nearest neighbors [26, 27]. Ring statistics are only useful for polymeric glasses and crystals [28–30]. The MRO topology was defined in earlier investigations of persistent homology analysis, but the chemical influence was missed [31, 32]. On the other hand, an analogy from DNA helps us to understand the significance of finding CMRO in liquids. While the statistical findings from X-ray diffraction assisted people in understanding the double helix structure of DNA reflecting MRO, the sequence of complementary base-pairing of DNA representing chemical order, lays the foundation for the variation of life. Thus, developing a new model that visualize the chemical medium-range order (CMRO) is what waits to be resolved.

The current work provides a simple mathematical model that, while ignoring the specifics, draws out the logical connections in complex glass-forming liquids. The concept is derived from Turing’s reaction-diffusion theory [33, 34], which explains how ordered patterns spontaneously develop from random complex systems with only an activator and an inhibitor and has been applied in many other fields, such as biology [35–37], chemistry [38–41], and 2D materials [42, 43]. In details, the elemental distribution of  $\text{Cu}_{50}\text{Zr}_{50}$  metallic glass is firstly visualized through continuous patterning, which is then confirmed as a Turing pattern. Secondly, persistent homology analysis is applied to study how temperature and interatomic potential influence the topology. Thirdly, a new criterion in addition to the negative  $\Delta H_{\text{mix}}$  is proposed, in order to separate the conditions for making metallic glasses from making crystals. Persistent homology analysis demonstrates that the relative magnitudes of the well depth of the interatomic potentials determines the medium-range structure of liquid alloys, which separates the products into categories including metallic glasses.

## RESULTS

### Modeling and its verification

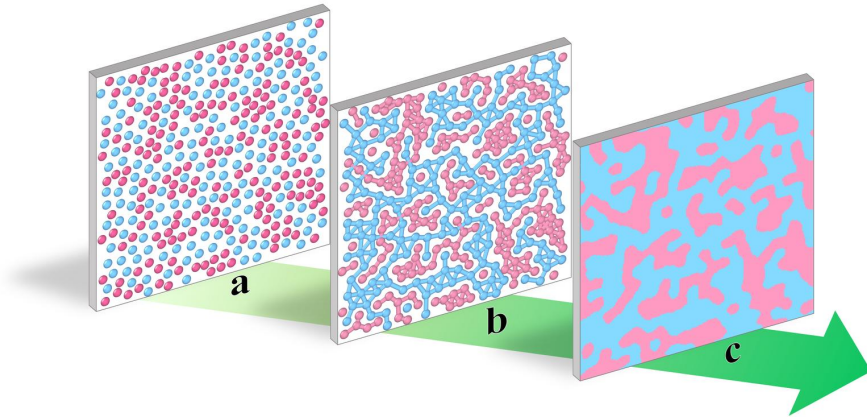


FIG. 1: **The structure of a 2D  $\text{Cu}_{50}\text{Zr}_{50}$  liquid.** (a) Red (for Cu) and blue (for Zr) balls highlighting the atomic positions. (b) Red (for Cu-Cu) and blue (for Zr-Zr) lines highlighting atomic bonds. (c) Continuous patterning highlighting the chemical ordering. The dimensions of the representation are  $5 \times 5 \text{ nm}^2$ .

A reformative microscopic depiction of metallic melts may help us grasp the CMRO.  $\text{Cu}_{50}\text{Zr}_{50}$ , a model MG-forming liquid, is used as an example. The model is a  $45.6 \times 45.6 \text{ nm}^2$  2D square

consisting of 29600 atoms. The sample was equilibrated at 2000 K after 1 ns relaxation. A portion of the square, i.e.,  $5 \text{ nm} \times 5 \text{ nm}$ , is cut out and shown in Fig. 1. Discrete dots emphasizing atomic positions of Cu (red dots) and Zr (blue dots) is presented in Fig. 1a. However, this presentation has the flaw of ignoring the atomic interactions that should take up the white space in Fig. 1a. As an alternative approach, the bondings of Cu-Cu (red lines) and Zr-Zr (blue lines) atomic pairs are demonstrated as the colored lines in Fig. 1b, from which different morphologies of Cu and Zr are revealed. Here, the Cu areas are separated, whereas the Zr areas are interconnected. Because Cu and Zr atoms have an equivalent atomic proportion of 50%, such morphological differences are inherent in chemistry. Further, by filling the white space of Fig. 1a using cubic interpolation (see more details in Fig. S1), the Cu and Zr areas are highlighted in the manner of Fig. 1c emphasizing the morphological difference between Cu and Zr. In this depiction, the minutiae of atomic position, atomic size and bonding are ignored, and the gist of chemical distribution is highlighted. These morphological traits are referred to as the chemical ordering of the  $\text{Cu}_{50}\text{Zr}_{50}$  liquid.

Figure 1c resembles a Turing pattern. To determine a Turing pattern, however, four requirements must be met: (i) the system consists of an activator that provides short-range positive feedback and an inhibitor that provides long-range negative feedback [34, 42, 44, 45]; (ii) the static image is obtained from dynamic evolution [36]; (iii) different initial states have no effects on the topological properties of the final structure [34, 35]; and (iv) the correlation length is fixed and independent on sample size [38, 39]. We now look into the validity of four criteria in the  $\text{Cu}_{50}\text{Zr}_{50}$  liquid.

The activator and inhibitor are determined by the interatomic potentials. Depending on the valley depth of the potential functions ( $|E_{\text{Zr-Zr}}|$  for Zr-Zr bond,  $|E_{\text{Cu-Zr}}|$  for Cu-Zr bond and  $|E_{\text{Cu-Cu}}|$  for Cu-Cu bond), the chemical affinity between atoms can be evaluated. For Cu-Zr, potential depth decreases in the order of Zr-Zr, Cu-Zr, and Cu-Cu. The formation of Zr-Zr and Cu-Zr bonds are active, promoting self-activation of Zr-Zr bonds and explaining the inter-connected morphology of Zr (Fig. 1c). The passive formation of Cu-Cu bonds, on the other hand, results in the long-range stimulation of Cu and the formation of Cu-rich regions. However, because the Cu-Zr bonds are energetically favored, meaning the creation of two Cu-Zr bonds at the cost of breaking Cu-Cu and Zr-Zr bonds are exothermic ( $\Delta H_{\text{mix}} = -23 \text{ kJ mol}^{-1}$  [1]), the Zr region is prevented from growing bigger, while the Cu regions are separated. In other words, Cu-Zr bonds inhibit Zr areas from growing over long distances, restricting Zr-Zr activation to short distances. Here,  $\Delta H_{\text{mix}} < 0$  functions in the prevention of Zr-Zr region enrichment. Fig. 2 summarizes the activation and

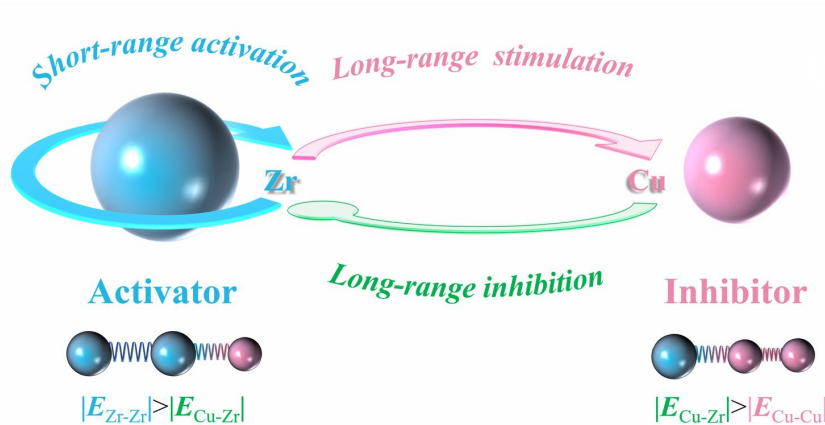


FIG. 2: **The formation mechanism of Turing pattern.** Here, the activator and inhibitor are Zr (blue balls) and Cu (red balls), respectively.

inhibition schemes of Cu and Zr.

A Turing pattern should be independent on the initial distribution of the activators and inhibitors. Otherwise, diffusion of the activator can create a pseudo-Turing pattern, driven by the chemical gradient of a similar pattern. The essence of a Turing pattern is the reaction between the activator and inhibitor that can erase the memory of the initial morphology. Starting from different initial distributions of  $\text{Cu}_{50}\text{Zr}_{50}$ , we found that the stabilized morphology is always a Turing pattern (Fig. 3). Though the final patterns are not exactly the same, the morphology of the blue and red areas are similar. Movies S1 and S2 also prove that the static Turing pattern of  $\text{Cu}_{50}\text{Zr}_{50}$  is obtained by dynamic evolution. Further, the size of the model system does not matter with the pattern. In another sample with dimension of  $22.7 \times 22.7 \text{ nm}^2$  consisting of 7360 atoms, the resulting pattern of Movie S2 and Fig. S3 are similar to those shown in Fig. 3. Thus, the morphology of  $\text{Cu}_{50}\text{Zr}_{50}$  liquid meets all the requirements of a Turing pattern.

**Pattern analysis through persistent homology: temperature effects**

The above-mentioned results of 2D  $\text{Cu}_{50}\text{Zr}_{50}$  liquid provide fundamentals of a Turing pattern. We now move on to a 3D  $\text{Cu}_{50}\text{Zr}_{50}$  liquid for topological analysis. A model system in a cube form of  $17 \times 17 \times 17 \text{ nm}^3$ , consisting of 256000 atoms, is simulated. A cube with a side length of 2 nm is cut out, highlighting the morphologies of Cu (red) and Zr (blue) as shown in Figs. 4a

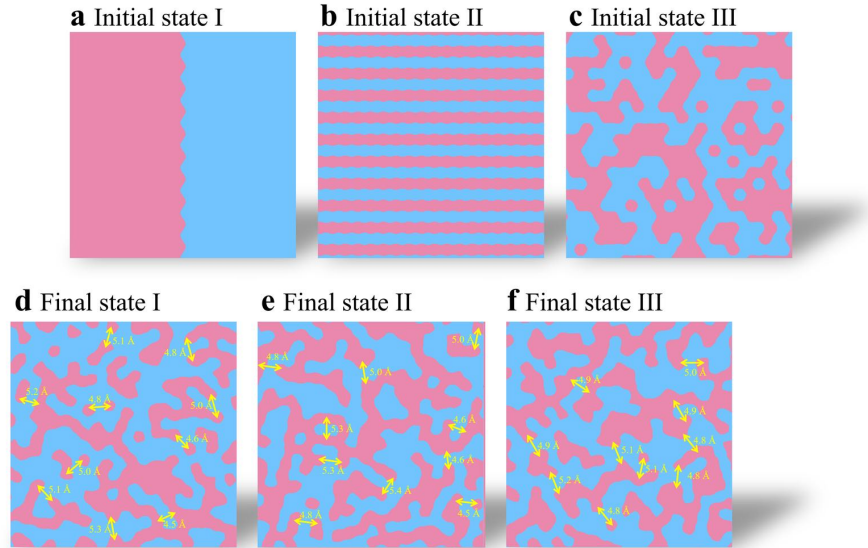


FIG. 3: **Morphology evolution of  $\text{Cu}_{50}\text{Zr}_{50}$  starting from three initial conditions including** (a) state I: Cu (red) and Zr (blue) are completely separated; (b) state II: Cu and Zr are arranged alternately in stripes; (c) state III: Cu and Zr are randomly arranged. The final states are presented in (d), (e) and (f), corresponding to (a), (b) and (c) after annealing the samples at 2000 K for (d) 20 ns, (e) 1 ns and (f) 1 ns. Yellow double-ended arrows visualize the characteristic lengths of the chemical medium-range order. The dimensions of the representation are  $5 \times 5 \text{ nm}^2$ .

and 4b. Here, Cu-Cu bonds are drawn when the interatomic spacing between Cu and Cu is within the cut-off distance ( $d_{\text{cut}}$ ), and  $d_{\text{cut}}$  is set as the locations of the first valleys in RDF (as shown in Fig. S2 and as collected in Table. S1). The Zr-Zr bonds are drawn in the same way. For better presentation, the bond width, i.e., the cylinder diameter, is set at 2 Å. A slice of 5-nm-long, 5-nm-wide and 5-Å-thick is cut out of the 3D cube, and the resulting patterns (Figs. 4c and 4d) resemble characteristics of 2D Turing patterns (Fig. 1c). A quantitative investigation of CMRO on a Turing pattern, particularly in 3D [46], however, necessitates persistent homology. Persistent homology is a topological method for extracting detailed properties in 3D structures [47]. It has been applied to extract not only structural short-range order but also structural medium-range order of oxide and metallic glasses [31, 32]. Unlike a former analysis [31] that neglected the element types and focused on the topology atomic structure for persistent homology analysis, the models applied here consider Cu and Zr atoms separately (Figs. 4e and 4f).

A persistent diagram (PD) is a birth-death time diagram obtained from persistent homology analysis. The birth time ( $t_b$ ) corresponds to the interatomic distance that forms a closed ring of

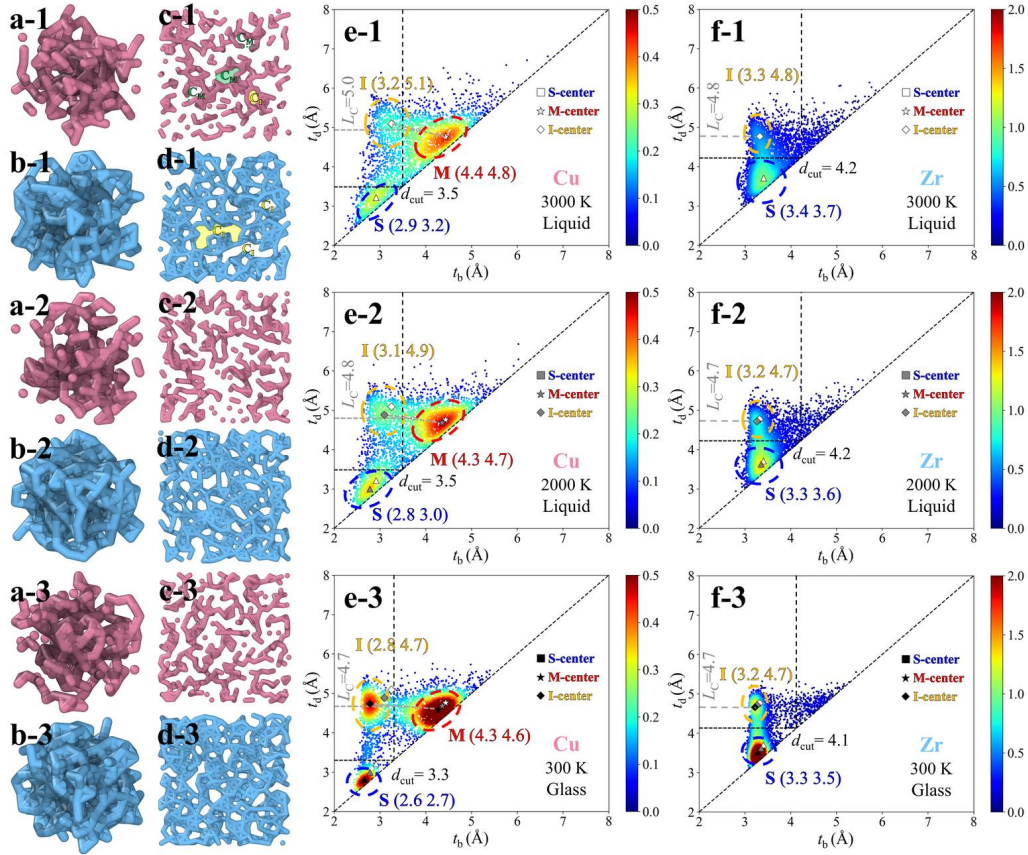


FIG. 4: Structure analysis of  $\text{Cu}_{50}\text{Zr}_{50}$  in 3D at (-1) 3000 K, (-2) 2000 K and (-3) 300 K, respectively. 3D structures of (a) Cu-Cu and (b) Zr-Zr bonds in  $\text{Cu}_{50}\text{Zr}_{50}$  ( $2 \times 2 \times 2 \text{ nm}^3$ ). Slice morphologies of (c) Cu-Cu and (d) Zr-Zr bonds ( $5 \times 5 \times 0.5 \text{ nm}^3$ ). Persistent diagrams of (e) Cu and (f) Zr.  $t_d$ ,  $t_b$ ,  $L_C$  and  $d_{\text{cut}}$  denote the death time, birth time, correlation length and cut-off distance, respectively.

bonds, while the death time ( $t_d$ ) is the interatomic distance that completely divides the ring by triangles (see **Methods** for more details). Three characteristics regions are found on the PDs of Cu. The S-region is located at (2.9 Å, 3.2 Å) representing ( $t_b$ ,  $t_d$ ), both are smaller than  $d_{\text{cut}}$  of 3.5 Å, indicating that the S-region represents the rings formed by the first-nearest neighboring Cu atoms. Here,  $d_{\text{cut}}$  is the abscissa of the trough of the first neighbor atom (see Fig. S2 and Tab. S1 for more details.). The M-region shown at (4.4 Å, 4.8 Å) represents the rings that are formed by the second-nearest neighboring Cu atoms. Examples are provided by “circle”  $C_M$  in Fig. 4c-1. The S- and M- regions have their  $t_b$  close to  $t_d$ . The I-region centered at (3.2 Å, 5.1 Å), reflects the rings that are formed by the first-nearest but terminated by the second-nearest neighboring Cu atoms. Examples are given by “circle”  $C_I$  in Fig. 4c-1, whose  $t_d$  is 59% greater than its  $t_b$ . Because it

includes a ring with  $t_d > d_{\text{cut}}$ , both I and M regions contain medium-range information. Fig. 4c-1 provides examples of S-, M- and I-regions. The S-region reflects rings formed by the first-nearest neighboring atoms at shorter length scale; the M-region is contributed by the rings established by connecting two separated Cu regions; the I-region represents rings formed by the first-nearest neighboring atoms at longer length scale. For the PD of Zr (Fig. 4f-1), two distinct zones are found. Within the  $d_{\text{cut}}$  of 4.2 Å, the S-region centers at (3.4 Å, 3.7 Å), reflecting short-range order. The I-region centers at (3.3 Å, 4.8 Å), reflecting medium-range order. The absence of an M-region distinguishes the PD of Zr from the PD of Cu. This indicates there are no rings produced by two separated Zr regions (Fig. 4d-1). This makes sense because all the Zr atoms are linked together. As a result, the existence of M-region established the distinction between Cu and Zr, reflecting chemical ordering at the medium range. Since no topological regions can be found beyond 5.1 Å (the maximum value of coordinates of all topological regions), the CMRO as revealed by the persistent homology limits to the second-nearest neighboring atomic distance. The mean  $t_d$  for I and M regions was used as the  $L_C$  of CMRO. Here, the  $L_C$  that defines CMRO is similar to both Cu and Zr atoms, of 5.0 Å on average. The width of the stripes or the spacing between the stripes of Turing pattern of MG (Fig. 1c) visualizes the  $L_C$ .

The temperature effects are further investigated. The Turing patterns exhibit similar features in both 3D (Figs. 4a and 4b) and 2D (Figs. 4c and 4d) at all three characteristic temperatures. However, the central colors and positions of the characteristic regions of their PDs differ. The central color of the regions warms up when the temperature is reduced from 3000 K to 2000 K, indicating that the liquid structure is more heterogeneous at the lower temperature. Additionally, the centers of all the regions shifts to the bottom left, indicating a compact local structure. At 300 K, the influence is increasingly pronounced as the regions highlighted by the dashed curves are nearly all filled by the central color, and the central positions are further reduced. Additionally, the boundaries separating S-, I- and M- regions are more defined in 300 K (Figs. 4e-3 and 4f-3) compared to 2000 K (Figs. 4e-2 and 4f-2). The  $L_C$  of CMRO, on the other hand, is slightly reduced to 4.7 Å at 300 K, in comparison with 4.8 Å at 2000 K and 5.0 Å at 3000 K. The structural ordering brought on by vitrification is reflected in a modest shortening in  $L_C$  and a narrower distribution of the characteristic local regions.



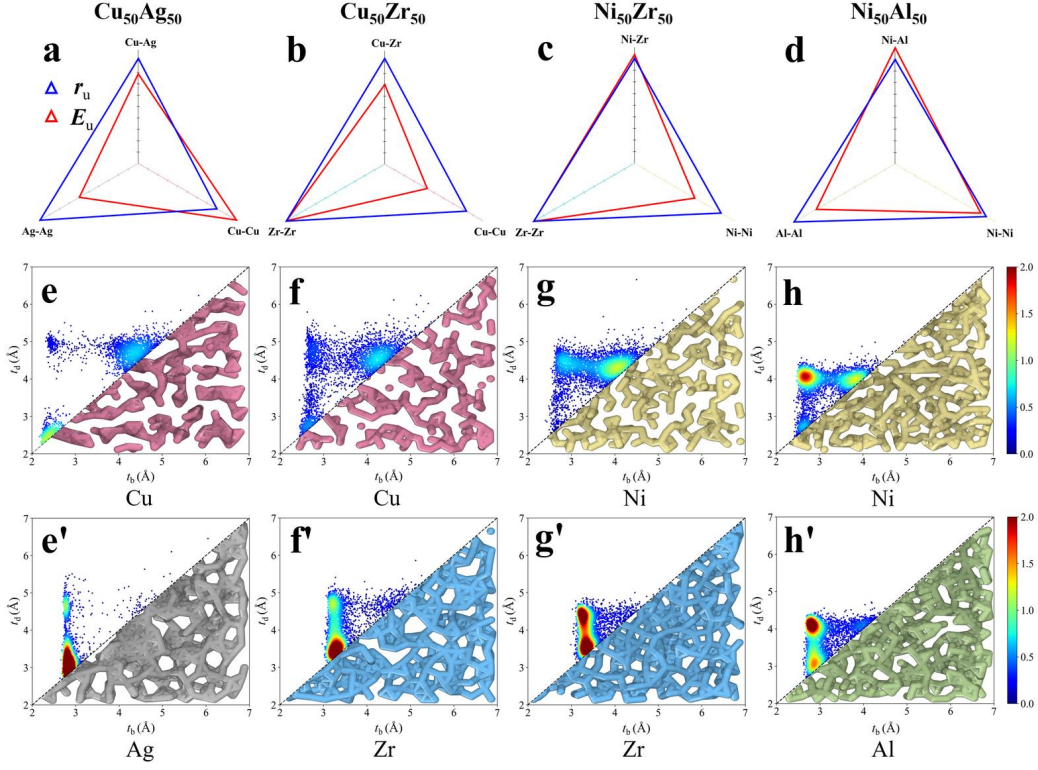


FIG. 5: **Structure analysis of different binary metallic glasses in 3D at 300 K.** Radar map characterizing the potential well of (a) Cu-Ag, (b) Cu-Zr, (c) Ni-Zr and (d) Ni-Al.  $E_u$  and  $r_u$  are normalized well energy and distance, respectively. Persistent diagrams and slice structures ( $5 \times 5 \times 0.5 \text{ nm}^3$ ) of (e)  $\text{Cu}_{50}\text{Ag}_{50}$ , (f)  $\text{Cu}_{50}\text{Zr}_{50}$ , (g)  $\text{Ni}_{50}\text{Zr}_{50}$  and  $\text{Ni}_{50}\text{Al}_{50}$ . Here, red, gray, blue, yellow and green represent Cu, Ag, Zr, Ni and Al respectively. The upper-left triangle is the persistent diagram, and the bottom-right triangle is the slice structures.

### Pattern analysis through persistent homology: Elemental effects

The effects of elemental types are studied on four equiatomic compositions, i.e.,  $\text{Cu}_{50}\text{Ag}_{50}$ ,  $\text{Cu}_{50}\text{Zr}_{50}$ ,  $\text{Ni}_{50}\text{Zr}_{50}$  and  $\text{Ni}_{50}\text{Al}_{50}$ . Their radar maps (Figs. 5a, 5b, 5c and 5d) represent variations in the normalized depth of potential well ( $E_u = \frac{E}{E_{\min}}$ ) and the normalized distance of potential well ( $r_u = \frac{r}{r_{\max}}$ ). Here,  $E$  and  $r$  respectively are the valley energy and distance of the potential function, while  $E_{\min}$  and  $r_{\max}$  respectively denote the lowest values of  $E$  reflecting the deepest valley and the highest  $r$  among all the alloy constituents. So, a stronger atomic binding is denoted by a larger  $E_u$ , and a shorter atomic bond is denoted by a smaller  $r_u$ . For  $\text{Cu}_{50}\text{Ag}_{50}$  (Fig. 5a) and  $\text{Cu}_{50}\text{Zr}_{50}$  (Fig. 5b), the  $r_u$ -triangles are comparable, but the  $E_u$ -triangles are different. The Cu-Cu

bond is the strongest in  $\text{Cu}_{50}\text{Ag}_{50}$  and the weakest in  $\text{Cu}_{50}\text{Zr}_{50}$ . Due to this, the S-region in the PD of Cu in  $\text{Cu}_{50}\text{Ag}_{50}$  (Fig. 5e) and the M-region in the PD of Cu in  $\text{Cu}_{50}\text{Zr}_{50}$  (Fig. 5f) are both the strongest. However, the PD of Ag in  $\text{Cu}_{50}\text{Ag}_{50}$  (Fig. 5e') resembles the PD of Zr in  $\text{Cu}_{50}\text{Zr}_{50}$  (Fig. 5f'), both containing S- and I-regions. Despite having various  $E_u$ -triangles, the similar topological properties are determined by the large potential well distance of Ag and Zr ( $r_u=1$ ). Given that the S-regions of Cu and Ag are both the warmest in color among their S-, I- and M-regions, it suggests that both the activator and inhibitor of  $\text{Cu}_{50}\text{Ag}_{50}$  are closely packed in topology (Figs. 5e and 5e'), forming a microscopic structure of phase separation, and creates difference from the topology of  $\text{Cu}_{50}\text{Zr}_{50}$  (Figs. 5f and 5f'). This is expected by the positive  $\Delta H_{\text{mix}}$  of Cu-Ag[1] and supported by experimental evidence [48, 49]. In the case of  $\text{Ni}_{50}\text{Zr}_{50}$ , it likewise possesses a similar  $r_u$ -triangle to  $\text{Cu}_{50}\text{Zr}_{50}$ , but the Ni-Zr bond is stronger than Cu-Zr bond in terms of  $E_u$  (Figs. 5b and 5c). As a result, the I-region is stronger in the PDs of both Ni and Zr (Figs. 5g and 5g') than it is in the PDs of both Cu and Zr (Figs. 5f and 5f'). The contradiction comes from Ni-Al which has a negative  $\Delta H_{\text{mix}}$  [1], and is a bad MG former as reported[50]. The Ni-Al bond is the strongest for  $\text{Ni}_{50}\text{Al}_{50}$  (Fig. 5d), therefore it tends to break Ni-Ni and Al-Al bonds. This rises the intensity of region I for both Ni and Al (Figs. 5h and 5h'), resulting in a binary crystal structure easily. Thus, the clues of glass formation resides in the intensity order of these PD regions.

## DISCUSSION

We now provide a schematic explanation (Fig. 6) on how chemical affinity influences the solid phase by using our data of equi-atomic binary alloys ( $\text{A}_{50}\text{B}_{50}$ ). These alloys have similar  $r_u$ -triangle but different combinations of interatomic potentials. Here, the chemical affinity is represented by the bond energy or the depth of the interatomic potentials ( $E < 0$ ). The absolute value of  $E$  of A-A bond,  $|E_{AA}|$ , is assumed greater than that of B-B, i.e.  $|E_{AA}| > |E_{BB}|$ .

If  $\Delta H_{\text{mix}} > 0$  occurs when  $|E_{AA}| > |E_{BB}| > |E_{AB}|$ , full immiscibility results in the sample. If  $\Delta H_{\text{mix}} > 0$  is obtained at  $|E_{AA}| > |E_{AB}| > |E_{BB}|$ , the system is partially miscible, and phase separation occurs. Here, B-B bonding is the least favored so that B-rich regions are hindered. On the other hand, A-A maintains its chemical affinity to bond with each other, which allows for A-A bond enrichment. Because A-B bond is stronger than the B-B bond, the A-rich regions are separated by the A-B bonds and surrounded by the passively formed B-rich regions, leading to phase separation. In the case of  $\Delta H_{\text{mix}} < 0$ , if it is acquired by  $|E_{AA}| > |E_{AB}| > |E_{BB}|$ , MGs

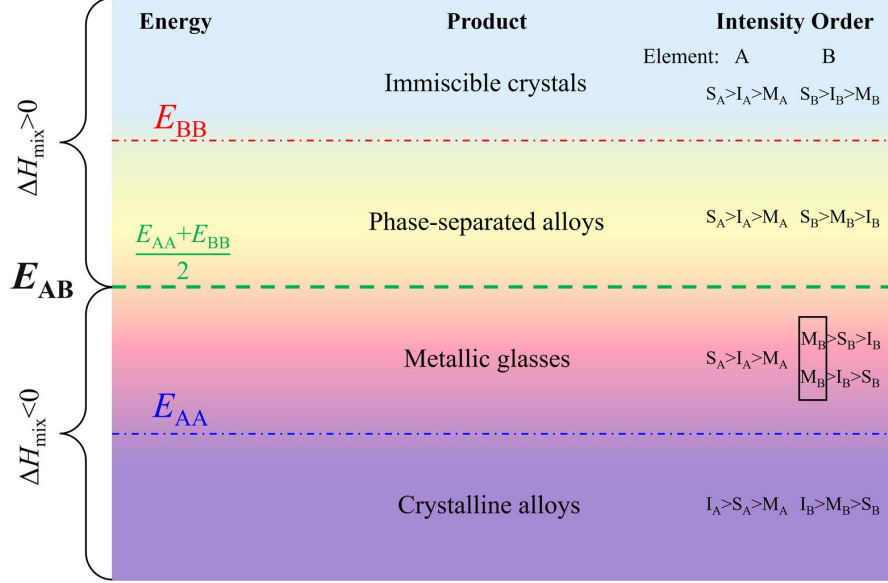


FIG. 6: Schematic diagram explaining how interatomic-potential energy depth ( $E_{AA}$ ,  $E_{BB}$  and  $E_{AB}$ ) and the intensity order of PD regions influence the products. Because the heat of mixing is  $\Delta H_{\text{mix}} = E_{AB} - \frac{(E_{AA} + E_{BB})}{2}$  [2, 51], the products are categorized into four sections, as separated by the dashed lines, according to the relative position of  $E_{AB}$ .  $S_A$  ( $S_B$ ),  $I_A$  ( $I_B$ ) and  $M_A$  ( $M_B$ ) represent the peak intensity of PD regions S, I and M of element A (or B), respectively.

are formed. The A-A bonding are still preferred as A-A bond has the strongest chemical affinity, but the growth of A-rich regions are strongly inhibited due to the growing influence of A-B bonds, making crystallization from A-rich regions difficult. If, on the other hand,  $\Delta H_{\text{mix}} < 0$  is obtained at  $|E_{AB}| > |E_{AA}| > |E_{BB}|$ , A-B bonding is energetically preferred so that A-B bond rich regions are grown. Crystalline binary alloys are likely produced at this condition.

The PD analysis provides a structural basis for these observations. When A and B atoms are fully immiscible, they are separatedly packed, and  $S_A$  and  $S_B$  are the strongest on their PDs. For phase separation,  $S_A$  and  $S_B$  are still the strongest because of the active enrichment of A atoms and the passive enrichment of B atoms. But, because the B-rich regions are passively formed, lacking connections to each other, a strong  $M_B$  resembling linkage of isolated regions in topology is obtained, giving rise to the relationship  $S_B > M_B > I_B$ . In the case of MG formation, A atoms are activators whose intensity order remains unchanged with  $S_A$  being the strongest. However, since B atoms are bonded more strongly with A atoms, the B-rich regions are capped by A atoms, leading to a spatial distribution of discrete islands. This then makes the  $M_B$  the strongest in its PD. Lastly for crystalline alloys,  $I_A$  and  $I_B$  are the strongest on their respective PDs, reflecting

the influence of strong A-B bonding. In this case, although  $\Delta H_{\text{mix}} < 0$  its magnitude does not promote MG formation but instead drives crystallization. Therefore, it is crucial to maintain  $|E_{\text{AA}}| > |E_{\text{AB}}| > |E_{\text{BB}}|$  while keeping a negative  $\Delta H_{\text{mix}}$  to create MGs. This is the criteria resolved from our topological analysis.

Finally, we highlight the broad implication this research may have. The basis of the model is solely dependent on the binding-energy order, regardless of the kind of objects or the size of the system. The fundamental building blocks can be applied to any objects like clusters or celestial entities in addition to atoms. In theory, any systems with competitive relations might have topological patterns in common. The different ways that the constituents engage with one another are what bring order out of chaos in spatial arrangement.

## CONCLUSION

This paper develops a new model to visualize the chemical medium range order of metallic glasses and answers why the magnitude of negative heat of mixing is irrelevant for glass formation. By shifting the microscopic presentation from discrete to continuous patterns, the present work discloses a Turing pattern with traits of dynamic development, starting-structure irrelevance, and sample-size independence. The patterns are quantitatively analyzed by persistent homology, where the topological difference of the constituents are revealed. Temperature and elemental type influence the topological properties shown in the persistent diagrams. Apart from a negative heat of mixing, the bonding energy of unlike species has to be set in the middle of the bonding energy of like species so that the intensity order of the persistent-homology regions is in favor of metallic-glass formation.

## METHODS

### MD simulations

Molecular dynamics (MD) simulation was conducted on LAMMPS [52] software. In this paper, the potential functions of Cu-Zr [53], Cu-Ag [54], Ni-Zr [55] and Ni-Al [56] were used. An isobaric and isothermal (NPT) ensemble was applied, and the system pressure was set to 0 with periodic boundary conditions. 2D  $\text{Cu}_{50}\text{Zr}_{50}$ , containing 29600 atoms in a  $45.6 \text{ nm} \times 45.6 \text{ nm}$  square, and all 3D samples, containing 256000 atoms in cubes, were modeled. The 2D and 3D

liquids were simulated by annealing the specimens at 2000 K and 3000 K for 1 ns to ensure that their liquid configurations were uniform. The 3D glass were simulated by quenching the liquids from 3000 K to 300 K at a cooling rate of  $2.7 \times 10^{13} \text{ K s}^{-1}$ .

### Persistent Homology

Persistent diagrams were constructed to analyze the topologies of different kind of atoms. The principles [31, 32] were to determine the birth time ( $t_b$ ) and death time ( $t_d$ ) of virtual rings. Due to the software's restriction on the number of atoms, 5000 atoms, carved from the center of the 3D specimen, were employed. All the persistent diagrams in this paper were obtained from the analysis of about 5000 atoms. In this work, Ripser toolkit [57] based on the Vietoris-Rips [58] was employed. In this toolkit, the virtual rings were born by connecting the virtual circles orbiting the atoms and were died when entirely divided by triangular loops. An example of  $t_b$  and  $t_d$  determination was given in Fig. S4.

### ACKNOWLEDGMENTS

This research was supported by the National Key Research and Development Plan (2018YFA0703603), the Strategic Priority Research Program of the Chinese Academy of Sciences (XDB30000000), the National Natural Science Foundation of China (51971239 and 92263103), and the Natural Science Foundation of Guangdong Province (2019B030302010). Correspondence and requests for materials should be addressed to Y.H.S. (ysun58@iphy.ac.cn). The data that support the findings of this study are available from the corresponding authors upon reasonable request.

- 
- [1] A. Takeuchi and A. Inoue, Classification of bulk metallic glasses by atomic size difference, heat of mixing and period of constituent elements and its application to characterization of the main alloying element, *Mater. Trans.* **46**, 2817 (2005).
  - [2] Y.-C. Hu, J. Schroers, M. D. Shattuck, and C. S. O'Hern, Tuning the glass-forming ability of metallic glasses through energetic frustration, *Phys. Rev. Mater.* **3**, 085602 (2019).
  - [3] Y.-C. Hu and J. Tian, Data-driven prediction of the glass-forming ability of modeled alloys by supervised machine learning, *Journal of Materials Informatics* **3**, 1 (2023).

- [4] Th. Voigtmann, A. Meyer, D. Holland-Moritz, S. Stüber, T. Hansen, and T. Unruh, Atomic diffusion mechanisms in a binary metallic melt, *Europhys. Lett.* **82**, 66001 (2008).
- [5] D. Holland-Moritz, F. Yang, J. Gegner, T. Hansen, M. D. Ruiz-Martín, and A. Meyer, Structural aspects of glass-formation in Ni-Nb melts, *J. Appl. Phys.* **115**, 203509 (2014).
- [6] Y. Q. Cheng and E. Ma, Atomic-level structure and structure–property relationship in metallic glasses, *Prog. Mater. Sci.* **56**, 379 (2011).
- [7] D. B. Miracle, A structural model for metallic glasses, *Nat. Mater.* **3**, 697 (2004).
- [8] A. Hirata, P. Guan, T. Fujita, Y. Hirotsu, A. Inoue, A. R. Yavari, T. Sakurai, and M. Chen, Direct observation of local atomic order in a metallic glass, *Nat. Mater.* **10**, 28 (2011).
- [9] H. L. Peng, M. Z. Li, W. H. Wang, C.-Z. Wang, and K. M. Ho, Effect of local structures and atomic packing on glass forming ability in  $\text{Cu}_x\text{Zr}_{100-x}$  metallic glasses, *Appl. Phys. Lett.* **96**, 021901 (2010).
- [10] J. Dana. Honeycutt and H. C. Andersen, Molecular dynamics study of melting and freezing of small Lennard-Jones clusters, *J. Phys. Chem.* **91**, 4950 (1987).
- [11] H. B. Yu, X. Shen, Z. Wang, L. Gu, W. H. Wang, and H. Y. Bai, Tensile plasticity in metallic glasses with pronounced  $\beta$  relaxations, *Phys. Rev. Lett.* **108**, 015504 (2012).
- [12] J. M. Cowley, X-Ray measurement of order in single crystals of  $\text{Cu}_3\text{Au}$ , *J. Appl. Phys.* **21**, 24 (1950).
- [13] B. E. Warren, X-ray Diffraction, New York: Dover Publications Inc. (1990).
- [14] G. Cargill and F. Spaepen, Description of chemical ordering in amorphous-alloys, *J. Non-Cryst. Solids* **43**, 91 (1981).
- [15] D. B. Miracle, W. S. Sanders, and O. N. Senkov, The influence of efficient atomic packing on the constitution of metallic glasses, *Philos. Mag.* **83**, 2409 (2003).
- [16] D. B. Miracle, E. A. Lord, and S. Ranganathan, Candidate atomic cluster configurations in metallic glass structures, *Mater. Trans.* **47**, 1737 (2006).
- [17] K. J. Laws, D. B. Miracle, and M. Ferry, A predictive structural model for bulk metallic glasses, *Nat. Commun.* **6**, 1 (2015).
- [18] J. D. Bernal, A geometrical approach to the structure of liquids, *Nature* **183**, 141 (1959).
- [19] J. D. Bernal, Geometry of the structure of monatomic liquids, *Nature* **185**, 68 (1960).
- [20] J. L. Finney, Random packings and the structure of simple liquids. I. The geometry of random close packing, *Proc. R. Soc. Lond. A.* **319**, 479 (1970).
- [21] J.-P. Hansen and McDonald, *Theory of Simple Liquids (Fourth Edition)* (Academic Press, Cambridge, MA, USA, 2013).

- [22] J. C. Dyre, Simple liquids' quasiuniversality and the hard-sphere paradigm, *J. Phys.: Condens. Matter* **28**, 323001 (2016).
- [23] S. R. Elliott, Origin of the first sharp diffraction peak in the structure factor of covalent glasses, *Phys. Rev. Lett.* **67**, 711 (1991).
- [24] S. Susman, K. J. Volin, D. L. Price, M. Grimsditch, J. P. Rino, R. K. Kalia, P. Vashishta, G. Gwanmesia, Y. Wang, and R. C. Liebermann, Intermediate-range order in permanently densified vitreous SiO<sub>2</sub>: A neutron-diffraction and molecular-dynamics study, *Phys. Rev. B* **43**, 1194 (1991).
- [25] G. N. Greaves and S. Sen, Inorganic glasses, glass-forming liquids and amorphizing solids, *Adv. Phys.* **56**, 1 (2007).
- [26] K. Nakamura and A. Ikawa, Medium-range order in amorphous selenium: Molecular dynamics simulations, *Phys. Rev. B* **67**, 104203 (2003).
- [27] Y. R. Guo, C. Qiao, J. J. Wang, H. Shen, S. Y. Wang, Y. X. Zheng, R. J. Zhang, L. Y. Chen, W.-S. Su, C. Z. Wang, and K. M. Ho, Bergman-type medium range order in amorphous Zr<sub>77</sub>Rh<sub>23</sub> alloy studied by ab initio molecular dynamics simulations, *J. Alloys Compd.* **790**, 675 (2019).
- [28] D. E. Polk, Structural model for amorphous silicon and germanium, *J. Non-Cryst. Solids* **5**, 365 (1971).
- [29] R. S. Le and V. Petkov, ISAACS – interactive structure analysis of amorphous and crystalline systems, *J. Appl. Crystallogr.* **43**, 181 (2010).
- [30] W. H. Zachariasen, The atomic arrangement in glass, *J. Am. Chem. Soc.* **54**, 3841 (1932).
- [31] Y. Hiraoka, T. Nakamura, A. Hirata, E. G. Escobar, K. Matsue, and Y. Nishiura, Hierarchical structures of amorphous solids characterized by persistent homology, *Proc. Natl. Acad. Sci. U.S.A.* **113**, 7035 (2016).
- [32] S. S. Sorensen, C. A. N. Biscio, M. Bauchy, L. Fajstrup, and M. M. Smedskjaer, Revealing hidden medium-range order in amorphous materials using topological data analysis, *Sci. Adv.* **6**, 10.1126/sciadv.abc2320 (2020).
- [33] T. Alan, The chemical basis of morphogenesis, *Phil. Trans. R. Soc. Lond. B* **237**, 37 (1952).
- [34] S. Kondo and T. Miura, Reaction-diffusion model as a framework for understanding biological pattern formation, *Science* **329**, 1616 (2010).
- [35] A. Nakamasu, G. Takahashi, A. Kanbe, and S. Kondo, Interactions between zebrafish pigment cells responsible for the generation of Turing patterns, *Proc. Natl. Acad. Sci. U.S.A.* **106**, 8429 (2009).
- [36] S. Kondo and R. Asai, A reaction-diffusion wave on the skin of the marine angelfish pomacanthus, *Nature* **376**, 765 (1995).

- [37] R. Asai, E. Taguchi, Y. Kume, M. Saito, and S. Kondo, Zebrafish leopard gene as a component of the putative reaction-diffusion system, *Mech. Dev.* **89**, 87 (1999).
- [38] V. Castets, E. Dulos, J. Boissonade, and P. De Kepper, Experimental evidence of a sustained standing Turing-type nonequilibrium chemical pattern, *Phys. Rev. Lett.* **64**, 2953 (1990).
- [39] Q. Ouyang and H. L. Swinney, Transition from a uniform state to hexagonal and striped Turing patterns, *Nature* **352**, 610 (1991).
- [40] J. Horvath, I. Szalai, and P. De Kepper, An experimental design method leading to chemical Turing patterns, *Science* **324**, 772 (2009).
- [41] Z. Tan, S. Chen, X. Peng, L. Zhang, and C. Gao, Polyamide membranes with nanoscale Turing structures for water purification, *Science* **360**, 518+ (2018).
- [42] Y. Fuseya, H. Katsuno, K. Behnia, and A. Kapitulnik, Nanoscale Turing patterns in a bismuth monolayer, *Nat. Phys.* **17**, 1031 (2021).
- [43] A. Fang, C. Adamo, S. Jia, R. J. Cava, S.-C. Wu, C. Felser, and A. Kapitulnik, Bursting at the seams: Rippled monolayer bismuth on NbSe<sub>2</sub>, *Sci. Adv.* **4**, eaaq0330 (2018).
- [44] H. Meinhardt and A. Gierer, Applications of a theory of biological pattern formation based on lateral inhibition, *J. Cell Sci.* **15**, 321 (1974).
- [45] H. Meinhardt and A. Gierer, Pattern formation by local self-activation and lateral inhibition, *Bioessays* **22**, 753 (2000).
- [46] T. Leppanen, M. Karttunen, K. Kaski, R. Barrio, and L. Zhang, A new dimension to Turing patterns, *Physica D* **168**, 35 (2002).
- [47] A. Patania, F. Vaccarino, and G. Petri, Topological analysis of data, *EPJ Data Sci.* **6**, 7 (2017).
- [48] H. Chen and J.-M. Zuo, Structure and phase separation of Ag–Cu alloy thin films, *Acta Mater.* **55**, 1617 (2007).
- [49] S. Nag, K. C. Mahdak, A. Devaraj, S. Gohil, P. Ayyub, and R. Banerjee, Phase separation in immiscible silver–copper alloy thin films, *J. Mater. Sci.* **44**, 3393 (2009).
- [50] C. Tang and P. Harrowell, Chemical ordering and crystal nucleation at the liquid surface: A comparison of Cu<sub>50</sub>Zr<sub>50</sub> and Ni<sub>50</sub>Al<sub>50</sub> alloys, *J. Chem. Phys.* **148**, 044509 (2018).
- [51] A. Takeuchi and A. Inoue, Calculations of mixing enthalpy and mismatch entropy for ternary Amorphous alloys, *Mater. Trans., JIM* **41**, 1372 (2000).
- [52] S. Plimpton, Fast parallel algorithms for short-range molecular dynamics, *J. Comput. Phys.* **117**, 1 (1995).



- [53] M. I. Mendelev, Y. Sun, F. Zhang, C. Z. Wang, and K. M. Ho, Development of a semi-empirical potential suitable for molecular dynamics simulation of vitrification in Cu-Zr alloys, *J. Chem. Phys.* **151**, 10.1063/1.5131500 (2019).
- [54] H. H. Wu and D. R. Trinkle, Cu/Ag EAM potential optimized for heteroepitaxial diffusion from ab initio data, *Comput. Mater. Sci.* **47**, 577 (2009).
- [55] S. Wilson and M. Mendelev, Anisotropy of the solid-liquid interface properties of the Ni-Zr B33 phase from molecular dynamics simulation, *Philos. Mag.* **95**, 224 (2015).
- [56] M. Mendelev, Interatomic Potentials Repository (2023), [Online; accessed 14. Mar. 2023].
- [57] C. Tralie, N. Saul, and R. Bar-On, Ripser.py: A lean persistent homology library for python, *The Journal of Open Source Software* **3**, 925 (2018).
- [58] N. Atienza, R. Gonzalez-Diaz, and M. Rucco, Persistent entropy for separating topological features from noise in Vietoris-Rips complexes, *J. Intell. Inf. Surf.* **52**, 637 (2019).

## Supplementary Materials for Turing Pattern and Chemical Medium-Range Order of Metallic Glasses

Song Ling Liu (刘松灵)<sup>1,2</sup>, Xin Yu Luo (罗新宇)<sup>1,2</sup>, Jing Shan Cao (曹景山)<sup>1,2</sup>, Zhao Yuan Liu (刘召远)<sup>3</sup>, Bei Bei Xu (许贝贝)<sup>4</sup>, Yong Hao Sun (孙永昊)<sup>1,2,5,✉</sup>, and Weihua Wang (汪卫华)<sup>1,2,5</sup>

*1. Institute of Physics, Chinese Academy of Sciences, Beijing, 100190, China.*

*2. School of Physical Sciences, University of Chinese  
Academy of Sciences, Beijing, 100190, China.*

*3. Shandong Computer Science Center (National Supercomputer Center in Jinan),  
Qilu University of Technology (Shandong Academy of Sciences), Jinan, Shandong, 250014, China.*

*4. Shanghai Institute of Microsystem and Information Technology,  
Chinese Academy of Sciences, Shanghai, 200050, China.*

*5. Songshan Lake Materials Lab, 523808, Dongguan, Guangdong, China and*

✉ Corresponding authors: ysun58@iphy.ac.cn

(Dated: May 10, 2023)

## SUPPORTING MOVIES

Movie S1 shows the pattern evolution of a 2D 29600-atom  $\text{Cu}_{50}\text{Zr}_{50}$  system at 2000 K with an initial state Cu and Zr are completely separated.

Movie S2 shows the pattern evolution of a 2D 7360-atom  $\text{Cu}_{50}\text{Zr}_{50}$  system at 2000 K, with an initial state when Cu and Zr are sliced into multilayers.

## SUPPORTING INFORMATION

A grid meshes the discrete representation of atomic positions. When the center of a Cu atom falls within a grid element, the grid element is indicated as 0, and when the center of a Zr atom falls within a grid element, it is indicated as 1. The remaining grid elements are filled by “cubic” interpolation of *griddata* code in Matlab 2018b. After that, the numerical matrix is binarized by setting the entries to 1 or 0 depending on whether the value is equal to and larger than or smaller than 0.5. As a result, a continuous pattern is created, with red denoting elements at values of 0 and blue denoting those at values of 1.

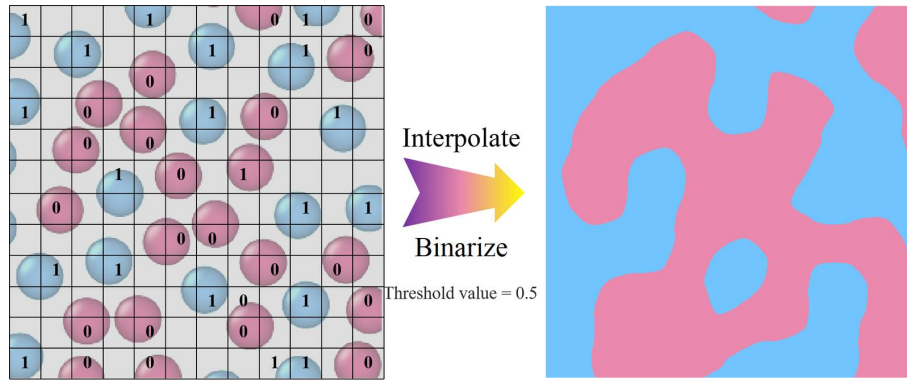


FIG. S1: **Schematic diagrams of the continuous process of 2D  $\text{Cu}_{50}\text{Zr}_{50}$  structure.**

Figure. S2 shows the  $g(r)$  of  $\text{Cu}_{50}\text{Zr}_{50}$  at different temperatures in 2D and 3D.

The positions of the 1<sup>st</sup> peak and its following valley are summarized in Table S1, where the positions of the valley defines the cut-off distance ( $d_{\text{cut}}$ ).

Time ( $t$ ) is visualized by the diameters of the circle centering each atom. When two circles are touched, a virtual bond is established with the bond-length equal to the diameters. In this work, Ripser toolkit[S1] based on the Vietoris-Rips[S2] was used. When the virtual bond is connected

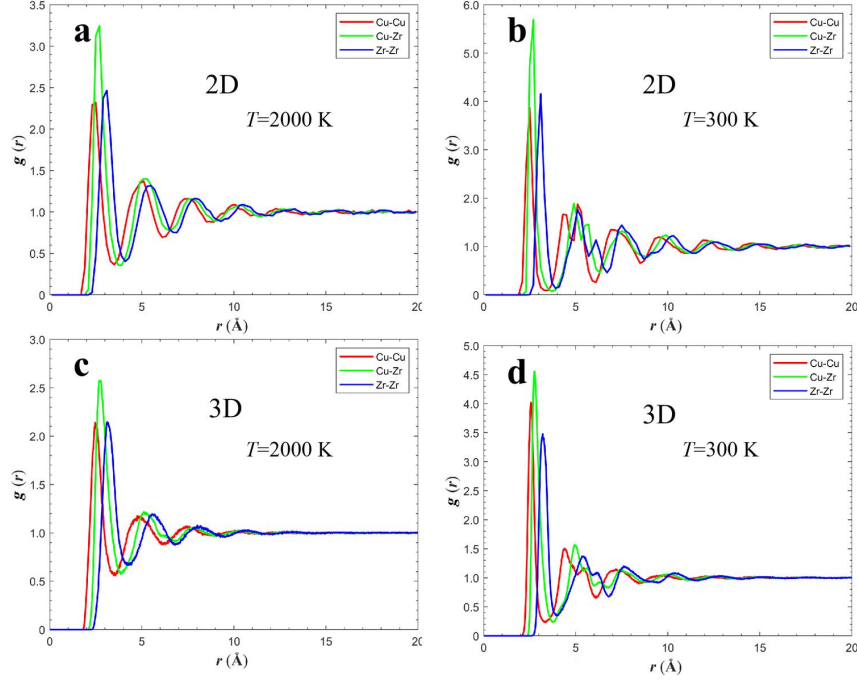


FIG. S2: **Radial distribution function (RDF)  $g(r)$  of 2D  $\text{Cu}_{50}\text{Zr}_{50}$  at (a) 2000 K, (b) 300 K and 3D  $\text{Cu}_{50}\text{Zr}_{50}$  at (c) 2000 K, (d) 300 K.**

Table S1: The locations of peaks and valleys in RDF under different circumstances.

State	Cu-Cu (Å)		Zr-Zr (Å)		Cu-Zr (Å)	
	peak	valley	peak	valley	peak	valley
<b>2D</b>						
300 K	2.5	3.4	3.0	4.0	2.6	3.8
2000 K	2.4	3.5	3.0	4.1	2.6	3.8
<b>3D</b>						
300 K	2.6	3.3	3.2	4.0	2.8	3.8
2000 K	2.5	3.5	3.2	4.2	2.7	3.8
3000 K	2.5	3.5	3.2	4.2	2.7	3.8

into a polygon (quadrilateral and above), a ring is born, this time is recorded as birth time ( $t_b$ ). When the polygon is completely split into a combination full of triangles, the ring is dead, and this time is denoted as death time ( $t_d$ ). For example, as shown in Fig. S4a, the  $C_1$  ring consisting of four neighboring bonds is created at  $t = d_1$ , yet ended at  $t = d_2$  because its ring structure is

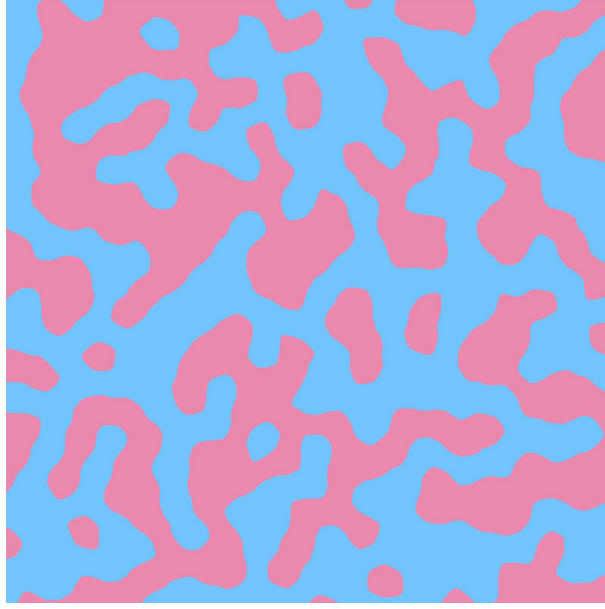


FIG. S3: Turing structure in a 7360-atom  $\text{Cu}_{50}\text{Zr}_{50}$  system after annealing it at 2000 K for 1 ns, which is consistent with that of 29600-atom system after annealing it at 2000 K (Fig. 3), indicating that the size of the system does not affect the morphology.

completely split into triangular loops.

Figure S4b is called persistent diagram (PD), which takes  $t_b$  and  $t_d$  obtained in Fig. S4a as abscissa and ordinate, respectively. In Fig. S4b, a time  $t = d_{\text{cut}}$  is selected, which divides the PDs into 3 dashed regions: blue, yellow and red, so called region D (death), region B (birth) and region F (future) respectively. When  $t = d_{\text{cut}}$ , as shown in Fig. S4a, the dead ring appears in region D, the undead ring appears in region B, and the ring about to be born appears in region F. For example, when  $d_3 \leq d_{\text{cut}} < d_4$ , the connection status of the virtual bond is the same as that of  $t = d_3$ . At this time, in Fig. S4a,  $C_1$  has been dead,  $C_2$  has been born but undead, and  $C_3$  has not yet been born.  $t_b$  and  $t_d$  of  $C_1$ ,  $C_2$  and  $C_3$  are drawn as blue, yellow and red points, respectively, in Fig. S4b, which fill into region D, B and F, respectively.

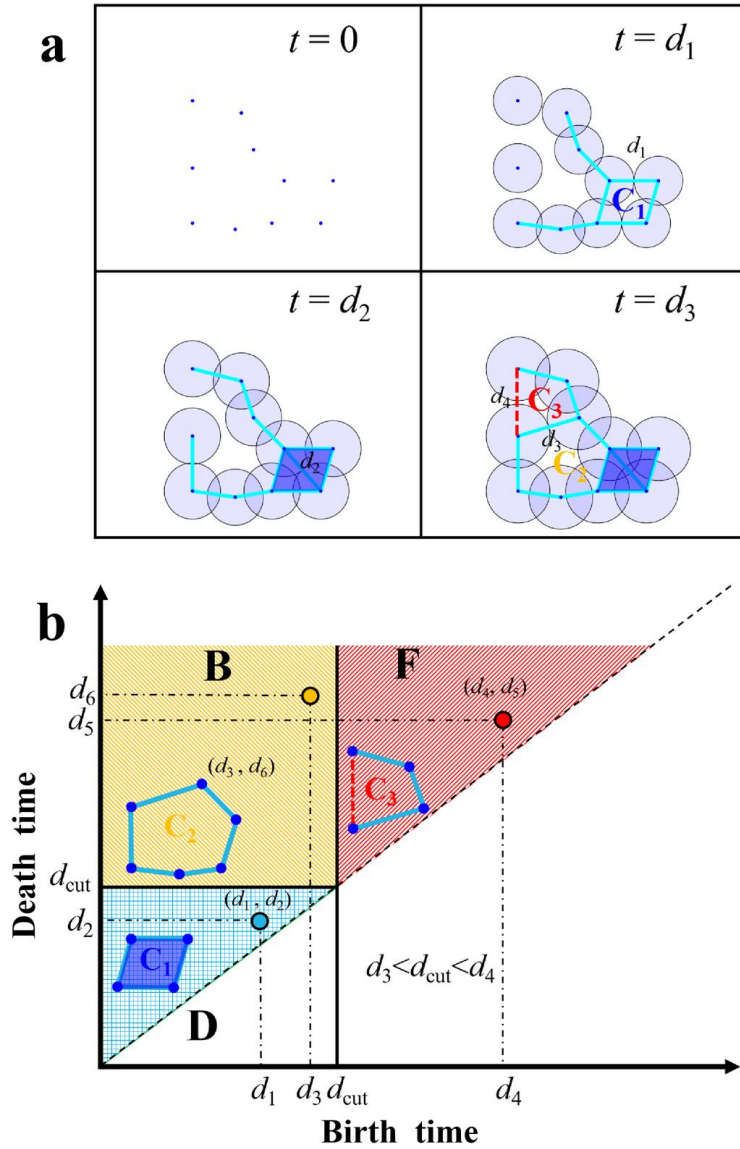


FIG. S4: **Schematic diagram of persistent homology.** (a) The schematic explaining the birth and death of the rings. Here,  $d$  is the interatomic distance. (b) Persistent diagram of (a). The blue, yellow and red area represent the death, birth and future regions, respectively.

- 
- [S1] C. Tralie, N. Saul, and R. Bar-On, Ripser.py: A lean persistent homology library for python, *The Journal of Open Source Software* **3**, 925 (2018).
- [S2] N. Atienza, R. Gonzalez-Diaz, and M. Rucco, Persistent entropy for separating topological features from noise in vietoris-rips complexes, *J. Intell. Inf. Surf.* **52**, 637 (2019).